Journal of Engineering Mathematics **33:** 175–200, 1998.

Freckle formation in a solidifying binary alloy

P. W. EMMS
James Rennell Division, Southampton Oceanography Centre, European Way, Empress Dock, Southampton SO14 3ZH, U.K. e-mail: p.emms@soc.soton.ac.uk

Received 30 October 1996; accepted in revised form 3 November 1997

Abstract. The effect of solutal convection on the unidirectional solidification of a binary alloy cooled from below is considered. Soon after the onset of solidification a mushy region often forms, and is accompanied by vigorous convection in the molten alloy above. In contrast, the fluid in the mush appears unaffected by the neighbouring flow and remains essentially quiescent. This work considers the nonlinear convective stability of the mush and determines a criterion for channelling in the mush to occur.

The basic state is a similarity solution, so that a quasi-static approximation must be applied in order to apply conventional stability theory. Moreover, although the model for solidification is relatively simple, an analytical expression for linear stability is not available. Thus the series of equations arising from the nonlinear stability analysis lead to a complicated set of symbolic and numerical calculations. Stable finite-amplitude solutions are found for Rayleigh numbers larger than critical for all values of the chosen superheat. The nonlinear solutions demonstrate the possibility of channelling within the mush dependent upon the strength of convection.

These finite-amplitude solutions are extended further by the calculation of a numerical solution of the model equations. The evolution of the stream function and the mass fraction is followed, the onset of convection and freckling can then be deduced from the numerical simulation. The onset of convection in the mush is found in terms of the mush Rayleigh number, and compares favourably with linear stability theory and experimental data. The onset of freckling is also given in terms of a Rayleigh number, but is sensitive to the initial conditions. This appears to explain the large disagreement found in experiments aimed at finding a criterion for freckling.

Key words: alloy solidification, nonlinear stability, freckling, moving-boundary problem, front-fixing.

1. Introduction

Freckles are one form of compositional segregation that can occur in castings of solidified binary alloys. They take the form of columns rich in one component of the alloy and with an equiaxed crystalline grain structure [1, pp. 251]. Copley *et al.* [2] established that freckles arise from the eventual solidification of flow channels (or chimneys) which often develop in the mushy region of a binary alloy. A mush is a region of mixed phase comprising of a complicated dendritic structure, and results from the morphological instability of the solid/liquid phase boundary [3]. Chimneys appear as channels of liquid alloy within the mush, and solidify at a later time than the surrounding phase mixture.

In the foundry a metal alloy solidifies in an ingot from a number of boundaries, so that the heat flux varies in direction. This makes it difficult to visualise solidification and complicates the flow in the melt. Consequently, in the laboratory a model alloy, such as aqueous ammonium chloride, is frequently used to investigate freckling and is only cooled on one boundary. This has the benefit of solidifying like a metal alloy, but it is transparent and so observation is easier. We shall focus our discussion on the unidirectional solidification of aqueous ammonium chloride.

Once aqueous ammonium chloride is sufficiently cooled, a mush soon forms, but the liquid remains essentially quiescent [4]. An important consequence of the phase diagram of this model alloy is the preferential incorporation of ammonium chloride molecules into the

crystalline lattice. Thus, in order to conserve solute, water is expelled at the solid–liquid interface and decreases the local density. This light fluid builds up in a boundary layer at the top of the mush due to limited liquid diffusion. Compositional convection is initiated in the completely liquid region when this boundary layer reaches a critical thickness [5].

The liquid region soon adopts a finger-like structure (*cf.* Turner [6, pp. 256]), while the mush remains stagnant. However, as the mushy layer thickens, a further convective instability occurs in the mush. Convection in the mush gradually increases leading to dendrite dissolution and thus preferred flow paths known as flow chimneys. This work builds upon Emms and Fowler's [7] work (hereafter referred to as EF) by constructing stable weakly nonlinear solutions and examining the influence of convection on porosity of the mush. These solutions are appropriate to the weakly convecting state in the mush. The quiescent state of the model is given by a similarity solution similar to that found by Worster [8]. Thus, we use a quasi-static approximation to determine the stability of the nonlinear solutions. A full numerical simulation of the solidification process is required to extend these solutions up to the onset of freckles. Experimental evidence [4] demonstrates that, in the absence of any convection, solidification is accurately described by a similarity solution. Thus, our conclusions should be directly applicable to observations.

Amberg and Homsy [9] have constructed weakly nonlinear solutions for the convective state in the mush. They considered finite-amplitude solutions to Worster's equations [10] for a *constant* solidification rate. The main limitations to their results were the adoption of the near-eutectic approximation and the assumption of a fixed boundary at the top of the mush. It was also assumed that the mush was thin, so that the basic steady state was linear to leading order. For two-dimensional convection it was found that subcritical rolls could occur in principle, although in an experiment they would be unlikely to be seen because of the narrow parameter range. Three-dimensional hexagonal structures were found to be transcritical for a much larger parameter range with branches corresponding to upflow at the centres or at the boundaries. Recent experiments by Tait, Jahrling and Jaupart [11] appear to confirm cells forming with an hexagonal planform. However, chimneys can be seen originating from the nodes of each hexagon, whereas the theory predicts upflow at the centre. Amberg and Homsy considered the stability of their finite-amplitude solutions only by way of analogy with similar nonlinear solutions of Rayleigh–Bénard flow. Anderson and Worster [12] have recently considered the stability of the nonlinear solutions of Amberg and Homsy's model. They found that stable hexagons with inflow and outflow at the centre were possible. Here we shall consider the stability of weakly nonlinear solutions perturbed from a time-dependent state.

Numerical simulations of freckle formation have previously been calculated by Neilson and Incropera [13, 14] and Felicelli, Heinrich and Poirier [15]. Neilson and Incropera considered the solidification of aqueous ammonium chloride whereas Felicelli *et al.* simulated the solidification of a lead-tin alloy. Both studies were based upon averaged models for which there was no need to explicitly track the mush/liquid interface. The interface position was determined *a posteriori* from the temperature field. There are a number of deficiencies to this approach. Both simulations were started from a quiescent state, and therefore one would usually expect finger convection above the mush to be initiated first. To resolve such convection accurately places a considerable restriction on the size of the mesh spacing. Both numerical studies only exhibited the mushy layer mode of instability [10], that is, no finger convection appeared in their results. Neilson and Incropera suggested that perturbations at the mush interface lead to channel formation. However, this could equally be the onset of fingering which, owing to the limits of the grid spacing, does not fully develop. Furthermore, the width of the channels that

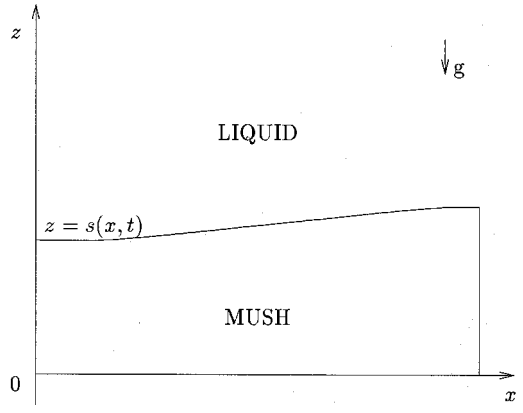

Figure 1. Schematic of a vertically solidifying alloy with a mushy region.

eventually formed depended upon the mesh size, which means that the numerical scheme does not accurately reflect the solution to the governing equations. Felicelli *et al.* do not mention whether there is any such dependence in their results. They predicted channels forming at the sides of the mold, if no initial perturbation was given to the solution. Thus, the spacing between freckles would appear to be determined by the width of the mold, contrary to the experimental observations of Tait and Jaupart [4].

The paper is divided into a number of sections. In Section 2 we introduce the nondimensionalised reduced model. The following two sections consider the stability of finite-amplitude perturbations to the similarity solution. In Section 5 we introduce the two numerical schemes used to solve the two-dimensional problem. Section 6 contains a description of a typical time series. The following section defines two parameters that can be used to determine the onset of convection and the onset of channelling in the mush from a time series. We are therefore able to compare our criteria with linear stability theory and experimental data. Section 8 contains some conclusions and suggestions for future work.

2. Model formulation

To describe freckle formation we shall use the reduced model developed in EF. Models for mushy regions now seem well established [5, 8, 16–17]. It seems unwise to reproduce the substantial amount of detail needed to describe the approximations made in the derivation of the reduced model. Full details can be found in Emms [18] and EF. To summarise, the model describes the unidirectional solidification of a binary alloy with eutectic solid forming below a mushy region of thickness s. The principal assumptions are thermodynamic equilibrium in the mush, infinite Lewis number in the mush, no solidification shrinkage, and the near-eutectic approximation (that is the initial composition is assumed to be near the eutectic). One consequence of this last assumption is that the solid/mush boundary moves slowly, and so we can assume the origin of our coordinate system is fixed on this interface. A schematic diagram of a solidifying alloy is shown in Figure 1. The notation is described in Table 1.

Table 1. Nomenclature

B	boundary-value operator
c	composition of the lighter component of the alloy
C_l	specific heat of the liquid alloy
d	macroscopic length scale
d_w	the convective cell width
F	far-field boundary
g	gravitational acceleration
h	spatial step size
k	wave number
L	latent heat
L_k	linear operator
N_x	number of intervals in the x-direction
N_z	number of intervals in the z-direction
s	position of liquid/mush interface
t	time
T	temperature
v	weakly nonlinear solution
x	horizontal coordinate
z	vertical coordinate
Z	scaled vertical cooordinate
Nondimensional parameters	
R	mush Rayleigh number
Δ_∞	superheat
$\mathcal{S}$	contribution of solidification to thermal budget
Subscripts	
c	onset of convection
E	eutectic
f	onset of freckling
i, j	grid position
l	liquid
s	solid/starting value
0	similarity solution
∞	far-field values
Greek letters	
α	similarity variable on interface
α_1, α_2	coeffs. to G-L eqn.
α_l^*	thermal expansion coefficient
β_l^*	solutal expansion coefficient
$\Delta\rho$	difference between the far-field liquidus density and that of the eutectic liquid
Δt	time step
ε	initial perturbation to quasi-static similarity solution
ϵ	initial perturbation to similarity solution used in numerical scheme
Γ	liquidus slope
κ_l	thermal diffusivity of the liquid phase
μ	liquid viscosity
ν	relaxation parameter
Π	permeability
ρ	density
ϕ	scaled solid mass fraction
ψ	stream function
τ	slow time scale
σ	growth of stream function
χ	liquid mass fraction
η	similarity variable
ζ	perturbed interface position
Superscripts	
n	nth time step
$*$	nondimensional variables or adjoint
0	values from the numerical model
N	values from the numerical model
$+$	liquid side of mush/liquid interface
$-$	mush side of mush/liquid interface

We nondimensionalise the spatial coordinates $\boldsymbol{x}$, time t, temperature T, stream function ψ and liquid mass fraction of mush χ using

$$\begin{aligned} &\boldsymbol{x} = d\boldsymbol{x}^*, \qquad t = \left(\frac{d^2}{\kappa_l}\right) t^*, \qquad T = T_L^\infty + (T_L^\infty - T_E)T^*, \\ &\psi = \kappa_l \psi^*, \qquad \chi = 1 - \left(\frac{c_E - c_\infty}{c_\infty}\right)\phi, \end{aligned} \tag{2.1}$$

where d is a macroscopic length scale (such as the height of the container holding the liquid alloy), κ_l is the thermal diffusivity of the liquid phase, T_L^∞ is the far-field liquidus temperature, and T_E is the eutectic temperature. A reference value for the density is ρ_l^0, gravity is g and

$$\Delta\rho = \rho_l^0[\beta_l^*(c_E - c_\infty) - \alpha_l^*(T_L^\infty - T_E)]$$

is the difference between the far-field liquidus density, and that of the eutectic liquid. Here α_l^*, β_l^* are thermal and solutal expansion coefficients, c_∞ is the far-field composition, and c_E is the eutectic composition. Henceforth we shall drop the asterisks on the nondimensional variables. Nondimensionalisation introduces three parameters that govern solidification and convection: the Rayleigh number

$$R = \frac{\Delta\rho g d \Pi_0}{\mu\kappa_l},$$

the superheat

$$\Delta_\infty = \frac{T_\infty - T_L^\infty}{T_L^\infty - T_E} \quad \text{and}$$

$$\mathcal{S} = 1 + \frac{L}{C_l \Gamma c_\infty},$$

which is related to the Stefan number and reflects the contribution solidification makes to the thermal budget. Here Π_0 is a permeability scale, μ is the viscosity, L is the latent heat, Γ is the liquidus slope, and C_l is the specific heat of the liquid phase. Typical values of these parameters for aqueous ammonium chloride given in EF are

$$R \sim 100, \qquad \Delta_\infty \sim 1{\cdot}6, \qquad \mathcal{S} \sim 1{\cdot}25. \tag{2.2}$$

In terms of the temperature T, composition of light component c, stream function ψ and the (scaled) solid mass fraction of mush ϕ the nondimensional model can be written as $z \to \infty$

$$T \to \Delta_\infty, \tag{2.3}$$

for $s < z < \infty$:

$$T_t + \psi_x|_{z=s} T_z = \nabla^2 T, \tag{2.4}$$

on $z = s(x,t)$:

$$\psi_n = 0, \qquad T = 0, \qquad T_n^+ = -c_n^-, \tag{2.5}$$

for $0 < z < s$:

$$\mathcal{S}[c_t + \psi_x c_z - \psi_x c_x] = \nabla^2 c, \qquad \nabla^2\psi = R c_x, \qquad \mathcal{S}\phi_t = \nabla^2 c, \tag{2.6}$$

on $z = 0$:

$$c = 1, \qquad \psi = 0, \tag{2.7}$$

where n is the normal to the mush/liquid interface. These are Equations (5.1)–(5.5) of EF.

We use the notation $[\,\cdot\,]^+_-$ to denote the jump in the quantity across the interface. The regions to which the model equations apply are shown in Figure 1. Equations (2.4) and $(2.6)_1$ express conservation of energy in the liquid and mush regions. The advective term in (2.4) requires some clarification. Emms and Fowler [7] found that finger-like convection above the mush can be described by an averaged energy equation. However, once convection has started in the mush, an additional mass flux will be superimposed on the finger structure. The advective term in (2.4) represents an approximation to this flux. As long as the interface remains fairly flat a purely vertical flux seems a reasonable approximation. In general, an averaged momentum equation governs the flow in the liquid, but for simplicity we do not consider this here. The remaining equations are Darcy's law $(2.6)_2$ and Equation $(2.6)_3$ which follows from conservation of species.

The temperature in the mush is given by the liquidus relation, which in nondimensional variables is

$$T = -c. \tag{2.8}$$

We are not concerned with the composition in the liquid region, as this uncouples in the model presented here.

In the absence of convection ($\psi = 0$), the reduced model has a similarity solution given by

$$\begin{aligned} &s_0 = 2\alpha\sqrt{t}, \qquad T_0 = \Delta_\infty \left[1 - \frac{\operatorname{erfc}\eta}{\operatorname{erfc}\alpha}\right], \\ &c_0 = 1 - \frac{\operatorname{erf}\mathcal{S}^{1/2}\eta}{\operatorname{erf}\mathcal{S}^{1/2}\alpha}, \qquad \phi_0 = c_0, \end{aligned} \tag{2.9}$$

where $\eta = z/2\sqrt{t}$ and the free-boundary location $\eta = \alpha$ is determined by

$$\frac{\Delta_\infty \,\mathrm{e}^{-\alpha^2}}{\operatorname{erfc}\alpha} = \frac{\mathcal{S}^{1/2}\,\mathrm{e}^{-\mathcal{S}\alpha^2}}{\operatorname{erf}\mathcal{S}^{1/2}\alpha}. \tag{2.10}$$

From this state we aim to construct weakly nonlinear solutions and examine their stability. However, we need to decide what we mean by stability, since the basic state is time dependent. Furthermore, nonlinear stability theory is a generalisation of linear stability theory, so we must specify just how the linear stability of a time-dependent state is defined. A similar problem arises in the study of a fluid layer whose basic temperature profile is changing with time. Such a situation can occur for example when one studies a growing thermal boundary layer [19]), or a fluid layer being cooled from above [20]. Little analytical progress has been made in this area, since the review by Homsy [21].

The nondimensionalised model is an implicit moving-boundary problem [22, pp. 19] because there is no explicit relationship for $\partial s/\partial t$ on the interface. We can make the problem explicit by differentiating one of the boundary conditions on $z = s$ with respect to time. However, this still leaves the problem of calculating the moving interface relative to a fixed mesh. One particularly attractive alternative is the fictitious-region method [23]. This is usually applied to moving-boundary problems where only one of the phases is in motion, that is solid/liquid Stefan problems. The method involves the construction of a set of equations valid

over the entire domain, which reduce in each phase to the relevant governing equations. Thus, the moving boundary is determined *a posteriori*. The construction of equations valid in both domains means that a set of discontinuous coefficients must be introduced. Although the fictitious-region method has been successfully applied to other Stefan problems, it is not the method we choose here. This is primarily due to the form of (2.4) which necessitates the introduction of a Heaviside function into the general governing equations.

Instead we apply a front-fixing transformation. This has the disadvantage that the form of the equations is complicated, but as a by-product yields an evolution equation for s.

3. Nonlinear stability

The complexities of nonlinear stability analysis limit our scope for dealing with the time-dependent basic state. Consequently, in this work we restrict ourselves to the concept of quasi-static stability. Thus we write

$$t = s_0^2 t^*, \qquad x = s_0 x^*, \qquad z = s_0 z^*, \qquad R_m = s_0 R, \qquad s = s_0 s^*, \tag{3.1}$$

where $s_0 = 2\alpha\sqrt{t}$ is the position of the interface given by a similarity solution and is considered fixed in time. The mush Rayleigh number is denoted by R_m. Under the quasi-static approximation the similarity solution (2.9) becomes (dropping the asterisks)

$$c_0 = 1 - \operatorname{erf}(\mathcal{S}^{1/2}\alpha z), \qquad c_0 = -\frac{\operatorname{erf}(\mathcal{S}^{1/2}\alpha z)}{\operatorname{erf}\mathcal{S}^{1/2}\alpha}\operatorname{erf}\mathcal{S}^{1/2}\alpha,$$

$$T_0 = \Delta_\infty\left[1 - \frac{\operatorname{erfc}(\alpha z)}{\operatorname{erfc}\alpha}\right]. \tag{3.2}$$

Perturbing the basic state we write

$$c = c_0 + \widehat{c}, \qquad T = T_0 + \widehat{T}, \qquad s = 1 + \widehat{\zeta}. \tag{3.3}$$

Dropping the hats, and substituting in Equations (2.3)–(2.7) we obtain the following set of equations

as $z \to \infty$:

$$T \to 0, \tag{3.4}$$

for $1 + \zeta < z < \infty$:

$$T_t + \psi_x|_{z=1+\zeta}(T_{0z} + T_z) = \nabla^2 T, \tag{3.5}$$

on $z = 1 + \zeta$:

$$\begin{aligned} &T_0 + T = 0, \qquad c_0 + c = 0, \qquad \psi_z - \zeta_x\psi_x = 0, \\ &T_{0z} + T_z - T_x\zeta_x = c_x\zeta_x - c_{0z} - c_z, \end{aligned} \tag{3.6}$$

for $0 < z < 1 + \zeta$:

$$\nabla^2\psi = R_m c_x, \qquad \mathcal{S}(c_t - \psi_z c_x + \psi_x(c_{0x} + c_z)) = \nabla^2 c, \tag{3.7}$$

on $z = 0$:

$$c = 0, \qquad \psi = 0. \tag{3.8}$$

We consider solutions to the above system of the form

$$\begin{aligned} &\psi = \varepsilon\psi_1 + \varepsilon^2\psi_2 + \cdots, \qquad T = \varepsilon T_1 + \varepsilon^2 T_2 + \cdots, \qquad c = \varepsilon c_1 + \varepsilon^2 c_2 + \cdots, \\ &\zeta = \varepsilon\zeta_1 + \varepsilon^2\zeta_2 + \cdots, \qquad R_m = R_c + \varepsilon^2 R_2 + \cdots, \end{aligned} \tag{3.9}$$

where R_c is the critical Rayleigh number given in the linear stability theory of EF, and the perturbation parameter $\varepsilon \ll 1$. Since we are expanding about the critical Rayleigh numnber, there is no perturbation expansion for the wave number; the sign of R_2 determines whether we consider solutions above or below the marginal stability curve (notice there is no εR_1 term in $(3.9)_5$ – see below).

To study the stability of these solutions we employ a multiple-scales analysis, that is we consider the slow time scale defined by

$$\tau = \varepsilon^2 t, \tag{3.10}$$

and examine slowly growing perturbations. This is at odds with the quasi-steady approximation as noted by Robinson [19, 24] for a growing thermal boundary layer. However, we proceed by considering stability to be 'defined' for this system relative to the steady state (3.2) obtained by using the quasi-steady approximation. The reason for choosing ε^2 and not ε to define the slow time scale is that by symmetry $R_1 = 0$ (or we find that for the solvability condition to be satisfied at order ε^2 requires $R_1 = 0$). Then, in order to have a nontrivial Ginzburg–Landau equation, we require $t \sim O(\varepsilon^2)$ to be the slow time. As in the work of EF, we assume an exchange of stabilities, so that

$$\psi = \psi(x, z, \tau), \qquad T = T(x, z, \tau), \qquad c = c(x, z, \tau), \qquad \zeta = \zeta(x, z, \tau).$$

Substituting the expansions (3.9) in (3.8) and collecting coefficients of powers of ε, we obtain the following series of problems

as $z \to \infty$:

$$T_k \to 0,$$

for $1 < z < \infty$:

$$\nabla^2 T_k - \psi_{kx}|_{z=1} T_{0z} = E_k,$$

on $z = 1$:

$$\psi_{kz} = A_k, \qquad T_k + T_{0z}\zeta_k = B_k, \qquad c_k + c_{0z}\zeta_k = C_k,$$

$$(T_{0zz} + c_{0zz})\zeta_k + T_{kz} + c_{kz} = D_k,$$

for $0 < z < 1$:

$$\mathcal{S}^{-1}\nabla^2 c_k - \psi_{kx} c_{0z} = F_k, \qquad \nabla^2\psi_k - R_c c_{kx} = G_k,$$

on $z = 0$:

$$c_k = 0, \qquad \psi_k = 0, \tag{3.11}$$

for $k = 1, 2, 3, \ldots$. The case $k = 1$ corresponds to the linear stability problem with $A_1 = B_1 = \cdots = G_1 = 0$. The coefficients $A_k, B_k, \ldots, G_k$ for $k = 2, 3$ are given in Emms [18].

4. The Ginzburg-Landau equation

Guided by the linear stability analysis of EF we restrict attention to the horizontal domain $0 < x < \pi/k_c$ where k_c is the critical wave number. We enforce the boundary conditions

$$c_x = T_x = \psi = 0,$$

at $x = 0, \pi/k_c$. Thus we force the convection cells to be of uniform width. More generally we can relax this assumption by introducing another larger space scale [25], [26]. However, this will complicate an already laborious solution procedure and is not of practical interest for finite solidification tanks, so we omit the possibility. Also note that we only consider perturbations with the critical wavenumber at leading order. Thus the nonlinear stability analysis presented here is much less general than the linear stability analysis presented in Emms [18], which considered arbitrary infinitesimal perturbations. Using a complete set of orthonormal functions (such as the eigenfunctions of the linear stability problem) it is theoretically possible for us to consider an arbitrary finite-amplitude perturbation. This yields an infinite set of ordinary differential equations to determine the stability [27, pp. 385]. Here we will instead only consider the nonlinear interaction of the most unstable mode in the hope that other modes have little effect on the stability of the solution.

If we write $v_i = (\psi_i, c_i, T_i, \zeta_i)^T$ then the $O(\varepsilon)$ problem $(k = 1)$ is

$$Lv_1 = \begin{pmatrix} \nabla^2\psi_1 - R_c c_{1x} \\ \mathcal{S}^{-1}\nabla^2 c_1 - c_{0z}\psi_{1x} \\ \nabla^2 T_1 - T_{0z}\psi_{1x}|_{z=1} \\ ((T_{0zz} + c_{0zz})\zeta_1 + T_{1z} = c_{1z})|_{z=1} \end{pmatrix} = 0, \tag{4.1}$$

and the boundary conditions on the interface $z = 1$ can be written

$$Bv_1 = \begin{pmatrix} \psi_{kz} \\ T_k + T_{0z}\zeta_k \\ c_k + c_{0z}\zeta_k \end{pmatrix} = 0. \tag{4.2}$$

The solution to (4.1) is of the form

$$v_1 = A(\tau) \begin{pmatrix} ik_c^{-1}\psi_{11} \\ c_{11} \\ T_{11} \\ \zeta_{11} \end{pmatrix} \mathrm{e}^{ik_c x}, \tag{4.3}$$

where the real part is understood to be under consideration, $A = A(\tau)$ can be taken to be a real function, and $(ik_c^{-1}\psi_{11}(z), c_{11}(z), T_{11}(z), \zeta_{11})^T$ is the eigenfunction given in EF.

The $k = 2$ problem can now be written

$$Lv_2 = M_2(v_1), \qquad Bv_2 = H_2(v_1), \tag{4.4}$$

where

$$M_2 = \begin{pmatrix} G_2(v_1) \\ F_2(v_1) \\ E_2(v_1) \\ D_2(v_1) \end{pmatrix}, \qquad H_2 = \begin{pmatrix} A_2(v_1) \\ B_2(v_1) \\ C_2(v_1) \end{pmatrix}.$$

Substituting (4.3) in M_2 and H_2 we arrive at expressions of the form

$$M_2 = A^2(m_{20} + m_{22}\,\mathrm{e}^{2ik_cx}), \tag{4.5}$$

$$H_2 = A^2(h_{20} + h_{22}\,\mathrm{e}^{2ik_cx}), \tag{4.6}$$

where $m_{20} = (0, f_{20}, e_{20}, d_{20})^T$, $m_{22} = (0, f_{22}, e_{22}, d_{22})^T$, $h_{20} = (-ia_{20}, b_{20}, \widehat{c}_{20})^T$, and $h_{22} = (-ia_{22}, b_{22}, \widehat{c}_{22})^T$. The hats on $\widehat{c}_{20}$, $\widehat{c}_{22}$ distinguish these variables from c_{20}, c_{22}. Notice that there is no solvability problem for (4.4), reflecting the fact that R_1 was set to zero earlier. The general solution to (4.4) is

$$v_2 = A^2\left(\begin{pmatrix} \psi_{20} \\ c_{20} \\ T_{20} \\ \zeta_{20} \end{pmatrix} + \begin{pmatrix} -i\psi_{22} \\ c_{22} \\ T_{22} \\ \zeta_{22} \end{pmatrix}\mathrm{e}^{2ik_cx}\right) + B\begin{pmatrix} ik_c^{-1}\psi_{11} \\ c_{11} \\ T_{11} \\ \zeta_{11} \end{pmatrix}\mathrm{e}^{ik_cx}, \tag{4.7}$$

where the real part is understood. The function $B = B(\tau)$ is determined by the solvability condition at $k = 4$. By examination of $A_3, B_3, \ldots, G_3$ we find the term containing B plays no part in the solvability condition for $k = 3$. As noted by Drazin and Reid [27, pp. 383], this is to be expected, since the term could equally be incorporated into the first order terms by modifying the definition of A. Henceforth, we shall drop this term from v_2. At this point it is convenient to introduce the operators L_n and B_n defined by

$$L_nv_{mn} = \begin{pmatrix} (D^2 - n^2k_c^2)\psi_{mn} + R_cnk_cc_{mn} \\ \mathcal{S}^{-1}(D^2 - n^2k_c^2)c_{mn} - nk_cc_{0z}\psi_{mn} \\ (D^2 - n^2k_c^2)T_{mn} - nk_cT_{0z}\psi_{mn}(1) \\ ((T_{0zz} + c_{0zz})\zeta_{mn} + DT_{mn} + Dc_{mn})|_{z=1} \end{pmatrix}, \tag{4.8}$$

$$B_nv_{mn} = \begin{pmatrix} D\psi_{mn} \\ T_{mn} + T_{0z}\zeta_{mn} \\ c_{mn} + c_{0z}\zeta_{mn} \end{pmatrix}, \tag{4.9}$$

where $v_{mn} = (\psi_{mn}, c_{mn}, T_{mn}, \zeta_{mn})^T$ and $D \equiv \mathrm{d}/\mathrm{d}z$.

At $k = 2$ we have two problems to solve

$$L_0v_{20} = m_{20}, \qquad B_0v_{20} = h_{20} \tag{4.10}$$

and

$$L_2 v_{22} = m_{22}, \qquad B_2 v_{22} = h_{22}. \tag{4.11}$$

The solution v_{20} to the system (4.10) represents the so-called mean motion at $O(\varepsilon^2)$. The numerical solutions to these problems will give

$$v_2 = A^2 \left[\begin{pmatrix} \psi_{20} \\ c_{20} \\ T_{20} \\ \zeta_{20} \end{pmatrix} + \begin{pmatrix} \psi_{22} \sin 2k_c x \\ c_{22} \cos 2k_c x \\ T_{22} \cos 2k_c x \\ \zeta_{22} \cos 2k_c x \end{pmatrix} \right]. \tag{4.12}$$

The problem at $k = 3$ can be written

$$L v_3 = M_3, \qquad B v_3 = H_3, \tag{4.13}$$

where

$$M_3(v_1, v_2) = \begin{pmatrix} g_{31}(v_1, v_2) \sin k_c x \\ f_{31}(v_1, v_2) \cos k_c x \\ e_{31}(v_1, v_2) \cos k_c x \\ d_{31}(v_1, v_2) \cos k_c x \end{pmatrix} + \begin{pmatrix} 0 \\ \dots \sin k_c x \\ \dots \sin k_c x \\ \dots \sin k_c x \end{pmatrix} + \text{higher harmonics} \dots,$$

$$H_3(v_1, v_2) = \begin{pmatrix} a_{31}(v_1, v_2) \\ b_{31}(v_1, v_2) \\ c_{31}(v_1, v_2) \end{pmatrix} \cos k_c x + \begin{pmatrix} \dots \\ \dots \\ \dots \end{pmatrix} \sin k_c x + \text{higher harmonics} \dots.$$

Consequently, we have a nontrivial solvability condition, which provides an evolution equation for A. Equation (4.13) is only solvable if there exists a solution to

$$L_1 v_{31} = m_3, \qquad B_1 v_{31} = h_3, \tag{4.14}$$

where $m_3 = (g_{31}, f_{31}, e_{31}, d_{31})^T$ and $h_3 = (a_{31}, b_{31}, \widehat{c}_{31})^T$. By the Fredholm alternative this has a solution if

$$\langle m_3, v_{31}^* \rangle = \mathcal{B}(h_3, v_{31}^*), \tag{4.15}$$

where $\mathcal{B}$ is a bilinear function arising from the nonhomogeneous boundary conditions on the interface. Here, the inner product is defined for real-valued vectors u and v by

$$\langle u, v \rangle = \int_0^1 (u_1 v_1 + u_2 v_2)\, \mathrm{d}z + \int_1^\infty u_3 v_3\, \mathrm{d}z + u_4 v_4. \tag{4.16}$$

In addition $v_{31}^* = (\psi_{31}^*, c_{31}^*, T_{31}^*, \zeta_{31}^*)$ is given by the solution to the homogeneous adjoint problem

$$L_1^* v_{31}^* = 0, \tag{4.17}$$

with boundary conditions on the interface

$$B_1^* v_{31}^* = 0. \tag{4.18}$$

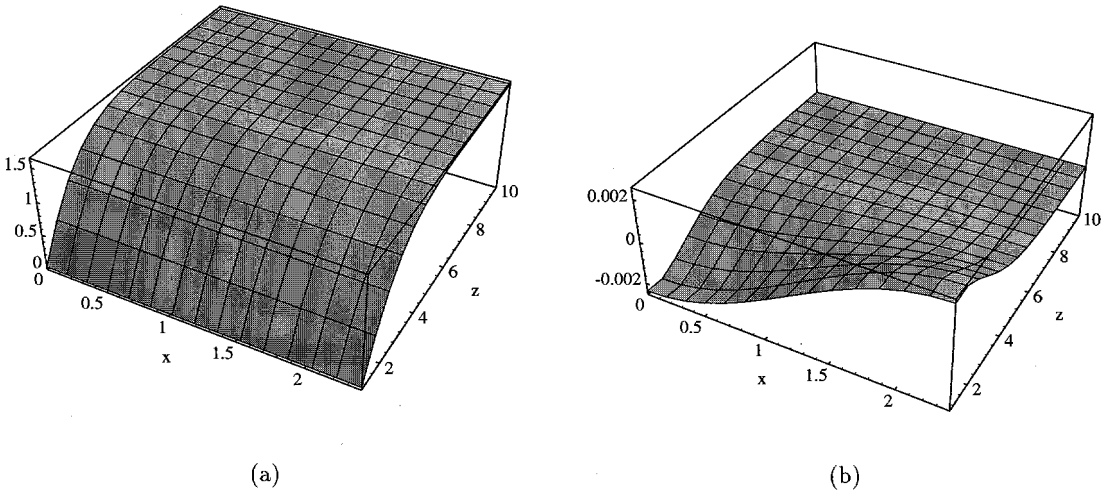

Figure 2 (a) The finite amplitude temperature T, and (b) the difference to the similarity solution $T - T_0$ for $R_2 = 1$ and $\varepsilon = 10^{-2}$.

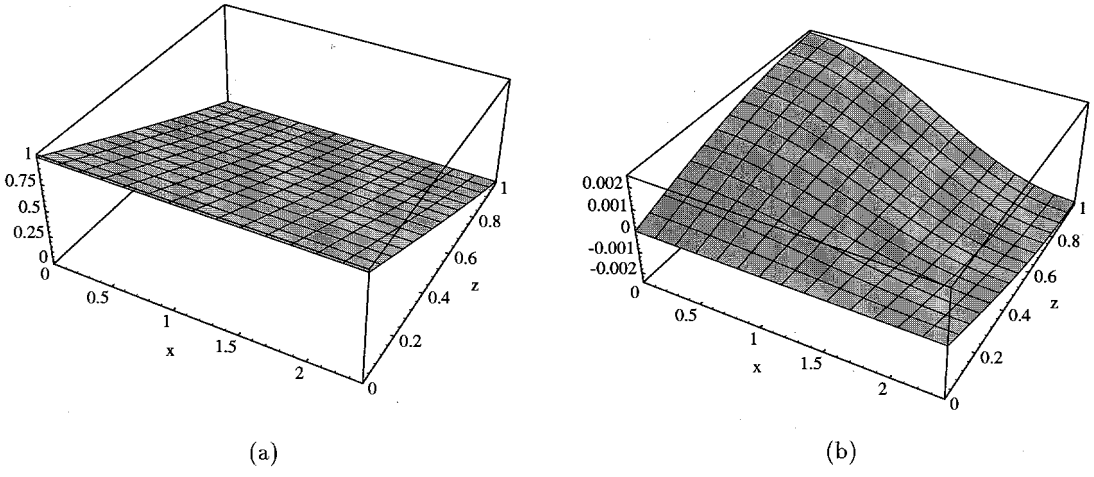

Figure 3 (a) The composition c, and (b) the difference to the similarity solution $c - c_0$ for $R_2 = 1$ and $\varepsilon = 10^{-2}$.

The exact forms of L_1^*, B_1^* and $\mathcal{B}$ can be found from integration by parts. The details are given in Emms [18].

Equation (4.15) is the Ginzburg-Landau equation. A great deal of computation will eventually lead to an equation of the more familiar form

$$\frac{\mathrm{d}A}{\mathrm{d}\tau} = \alpha_1 R_2 A + \alpha_2 A^3, \tag{4.19}$$

where α_1, α_2 must be determined numerically. From EF we must have $\alpha_1 > 0$, since we have instability for $R > R_c$. If $\alpha_2 > 0$, the bifuraction from the basic state is said to be subcritical, whereas, if $\alpha_2 < 0$, the bifurcation is supercritical. If the bifurcation is subcritical, we would expect experimental and numerical results to predict the onset of convection at an

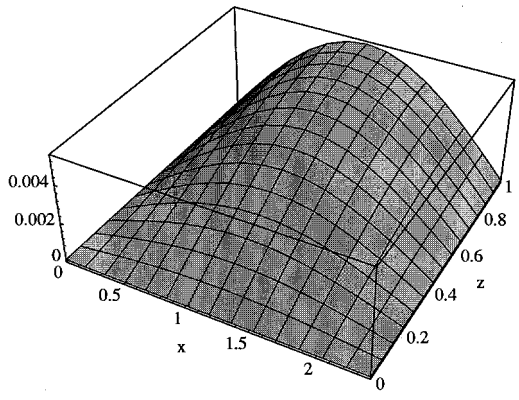

Figure 4. The stream function ψ for $R_2 = 1$ and $\varepsilon = 10^{-2}$.

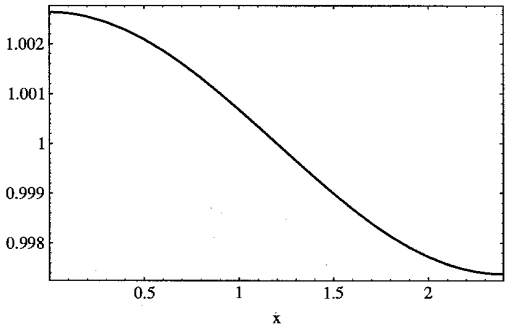

Figure 5. The interface position s for $R_2 = 1$ and $\varepsilon = 10^{-2}$.

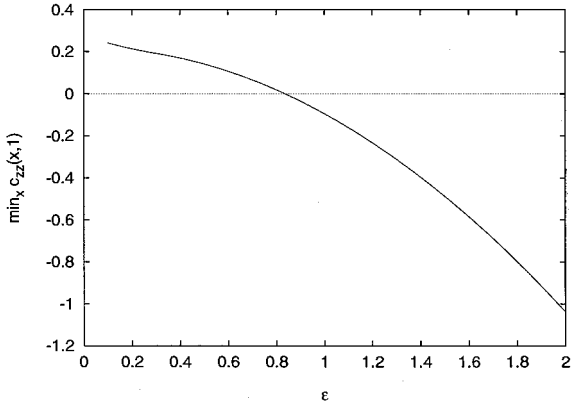

Figure 6. The range of validity of the weakly nonlinear solution.

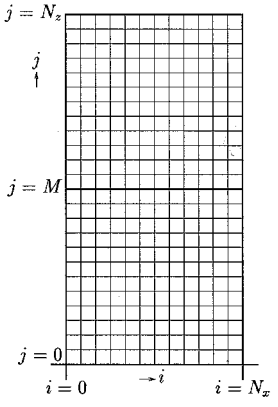

Figure 7. The finite difference grid shown for the representative values $h = \frac{1}{12}$, $F = 2$.

earlier time than predicted by linear stability. Also, initial conditions would play an important part in the determination of the critical time. If the bifurcation is supercritical, the instability should be relatively insensitive to initial conditions, assuming the quasi-static approximation is reasonable.

We performed two sets of calculations using a far-field approximation $z = F = 10$, 20. The calculations are rather complicated since the solution to the linear stability problem can only be found numerically. The details of the calculation can be found in Emms [18]. To summarise, the problem requires the numerical solution of the linear stability problem (4.3), the two linear systems at $k = 2$: (4.10), (4.11), and the adjoint problem (4.17). These solutions then give the coefficients of (4.19) when substituted in (4.15).

Using the values in (2.2), we observed that both numerical computations for $F = 10$, $F = 20$ gave the values of α_1 and α_2 in (4.19) as

$$\alpha_1 = 0{\cdot}35, \qquad \alpha_2 = -0{\cdot}045. \tag{4.20}$$

The results indicate a supercritical bifurcation, with the approximation of the infinite boundary having no discernible effect. Thus, a stable finite-amplitude solution exists for $R_2 > 0$ with equilibrium amplitude

$$A_{eq} = \sqrt{-\frac{\alpha_1 R_2}{\alpha_2}}. \tag{4.21}$$

This solution is plotted in Figures 2–5 for $R_2 = 1$ and $\varepsilon = 10^{-2}$, which gives $A_{eq} = 2{\cdot}78$. The stream function is positive which indicates that convection proceeds in a clockwise direction in the mush. This increases the composition on the left-hand side of the cell (near $x = 0$) and decreases composition on the right (Figure 3b). Without the quasi-steady approximation, the (scaled) mass fraction of solid is related to the composition by

$$\phi_t = \frac{\mathrm{d}c}{\mathrm{d}t} = \mathcal{S}^{-1}\nabla^2 c. \tag{4.22}$$

From the equilibrium compositional field (Figure 3) we can see that $\psi_x c_z$ is negative on the left of the cell and positive on the right. Therefore, freezing is inhibited on the left and promoted on the right. The mush/liquid interface is located on the isotherm $c = 0$. Consequently, the interface advances on the left side of the cell as shown in Figure 5.

The size of ε measures the strength of convection. As ε is increased, so the solid fraction on the left side of the cell is diminished until eventually $\phi < 0$ inside the mush. Consequently, the theory predicts a channel forming in the mush near the liquid interface. Thus $\phi < 0$ is our criterion for channelling and ultimately freckle formation. It is also the metallurgical condition [16] evaluated on the mush-liquid interface, since if $\phi < 0$ at $z = s$ then from (4.22), $\mathrm{d}T/\mathrm{d}t > 0$ at $z = s$.

Once $\phi < 0$, our model is no longer valid, and so there is a bound on the validity of the finite amplitude solutions. We can determine this bound by noting on $z = s$, $\phi_t = \mathcal{S}c_{zz}$. Of course, we present our equilibrium solution in terms of variables defined using the quasi-steady approximation (3.1). However, we only need the sign of c_{zz}. Therefore, since the amplitude of the nonlinear solution increases monotonically to the equilibrium value A_{eq}, we can use $c_{zz} < 0$ at $z = s$ as the bound. In Figure 6 we plotted $\min_x c_{zz}(x, 1)$ for $0 \leqslant x \leqslant \pi/kc$ against ε using the equilibrium finite-amplitude solution for $R_2 = 1$. At $\varepsilon = 0{\cdot}82$, ϕ becomes negative and the finite-amplitude solution has no physical meaning. As we require $\varepsilon \ll 1$ to perform the weakly nonlinear analysis, this bound does not restrict the range of solutions further. However, it does mean that we cannot use the nonlinear solution to give a criterion for freckling. Indeed, such a criterion would be rather unsatisfactory as it would be given in terms of the fluid velocity which is an integral part of the problem. We can resolve this difficulty by solving the reduced model numerically and we address this problem next.

5. The numerical solution

We fix the interface on $Z = 1$ by applying the transformation

$$z = sZ. \tag{5.1}$$

This disrupts the structure of the equations since $s = s(x, t)$. If we define the width of the horizontal domain as d_w, then it is convenient to rescale

$$x = d_w \widehat{x}, \qquad t = d_w^2 \widehat{t}, \tag{5.2}$$

in an analogous manner to the linear stability analysis of EF. Generally we hope to set d_w close to $\lambda_c/2$ where λ_c is the critical wavelength given by linear stability theory. This should mean that the most unstable mode (predicted by linear stability) will be excited during the numerical simulation, and therefore the results can be compared. If we just set $d_w = 1$, then linear stability predicts that the onset of convection is delayed. Furthermore, as time progresses, the mush interface advances, but the width of the cell remains fixed. Thus, the aspect ratio increases, as does the minimum wave number that can be excited, which further delays the onset of convection. Consequently, the situation may arise in which convection never occurs for sufficiently small d_w. Note that, if d_w is made sufficiently large, multi-cellular convection is expected, and d_w is then not the width of a *cell*. Henceforth we shall drop the hats on x and t. We also need some additional boundary conditions on $x = 0, 1$, which we take to be periodic, that is

$$\psi = T_x = s_x = 0. \tag{5.3}$$

At $t = 0$ there is a singularity in the interface velocity $\dot{s} = \alpha/\sqrt{t}$. Therefore, we start the numerical simulation using the similarity solution at time $t = t_s < t_c$, where $t_c = t_c(\Delta_\infty)$ is the time when convection is initiated according to the linear stability analysis of EF. The effect of an initial perturbation to the non-convective state can be assessed if the initial conditions are taken as

$$\begin{aligned} &s = s_0 + \epsilon \cos \pi x, \qquad \psi = \epsilon \sin \pi x \sin(\pi Z/2), \\ &T = T_0 - \epsilon \cos \pi x \sin \pi Z, \qquad \phi = \phi_0 - \epsilon \cos \pi x \sin \pi Z, \end{aligned} \tag{5.4}$$

at $t = t_s$, where ϵ represents the size of the initial perturbation. Although (5.4) satisfies the boundary conditions to the problem, it is obviously not a solution. Consequently, we expect there will be a short transient in which the numerical scheme adjusts to the solution of the equations. It is expected that the perturbation will initially decrease and then increase, once convection has been initiated.

The application of the front-fixing transformation (5.1) considerably disrupts the structure of the full equations. Consequently, we shall only consider two numerical schemes, both of which approximate the time derivative with a backward difference. For simplicity we assume a square mesh with the number of intervals in the x-direction and the z-direction given by

$$N_x = \frac{1}{h}, \qquad N_z = \frac{F}{h}, \tag{5.5}$$

respectively, where $z = F$ is the approximation to the infinite boundary, and h is the step size. The finite-difference grid is shown in Figure 7 with the interface lying on $j = M$. Using the usual notation, we observe that the quantity $T^n_{i,j}$ represents the approximation to $T(ih, jh, n\Delta t)$. The first and second spatial derivatives are approximated by means of central differences, and so the truncation error is $O(\Delta t + h^2)$. The front-fixing transformation also introduces mixed derivatives. We approximate these terms using a non-centred seven-point molecule of the form

$$\frac{\partial^2 T}{\partial x \partial Z} \approx \frac{T^n_{i,j+1} - T^n_{i-1,j+1} + T^n_{i+1,j} - 2T^n_{i,j} + T^n_{i-1,j} - T^n_{i+1,j-1} + T^n_{i,j-1}}{2h^2} \tag{5.6}$$

In the first numerical scheme the interface position and the convective derivatives are calculated from the temperature field at the old time step. Thus, the finite-difference equations

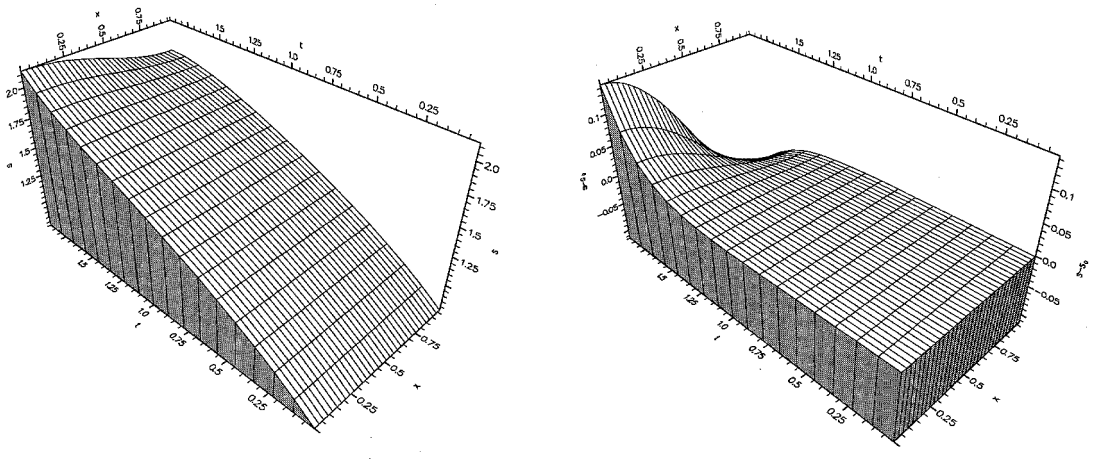

(a) (b)

Figure 8. The evolution of the mush/liquid interface for $d_w = 2{\cdot}0$, $\Delta_\infty = 1{\cdot}6$, $\Delta t = 10^{-3}$, $h = \frac{1}{32}$, $\epsilon = 10^{-5}$, $t_s = 0{\cdot}1$ where (a) shows $z = s(x,t)$, and (b) shows the difference to the similarity solution s_0.

are linear in variables at the new time step. We call this the lagged scheme. The second scheme uses the temperature field at the new time step, and so requires successive substitution. *A priori* we expect the second, fully implicit scheme to describe the coupling between s, T and p more accurately. Both schemes lead to a system of difference equations of the same structure.

6. A typical time series

In this section we describe a simulation for a typical value of the superheat $\Delta_\infty = 1{\cdot}6$, and $\mathcal{S} = 1{\cdot}25$ using the fully implicit scheme. Linear stability theory (EF) predicts convective instability at $t_c = R_c^2/4\alpha^2 R^2 d_w^2$, which for $R = 10$ and $d_w = 2$ gives $t_c = 0{\cdot}286$. We take the width of the horizontal domain to be $d_w = 2$ because the critical wavelength predicted by linear stability is

$$\lambda_c = 2\pi R_c / k_c R. \tag{6.1}$$

One convective cell is expected to have a width $\lambda_c/2$, and for the values above, $\lambda_c = 3{\cdot}57$. The simulation was started at time $t_s = 0{\cdot}1$, and the initial perturbation to the similarity solution was set to $\epsilon = 10^{-5}$, in an effort to minimize noise at the beginning of the simulation. The mesh size h, and the time step Δt were specified as $h = \frac{1}{32}$, and $\Delta t = 10^{-3}$. The results are displayed in Figures 8–10.

The evolution of the mush/liquid interface is shown in Figure 8(a), and the deviation from the similarity solution in Figure 8(b). It can be seen from these figures that there is little deviation from the similarity solution, but towards the end of the simulation the interface advances more quickly near $x = 0$, and is slowed near $x = 1$. As with the nonlinear solutions this corresponds to clockwise convection in the mush carrying colder, more concentrated liquid up the left-hand side of the cell, and therefore promoting solidification. Conversely, on the right-hand side of the cell, warmer less concentrated fluid from the liquid region enters the mush and inhibits solidification.

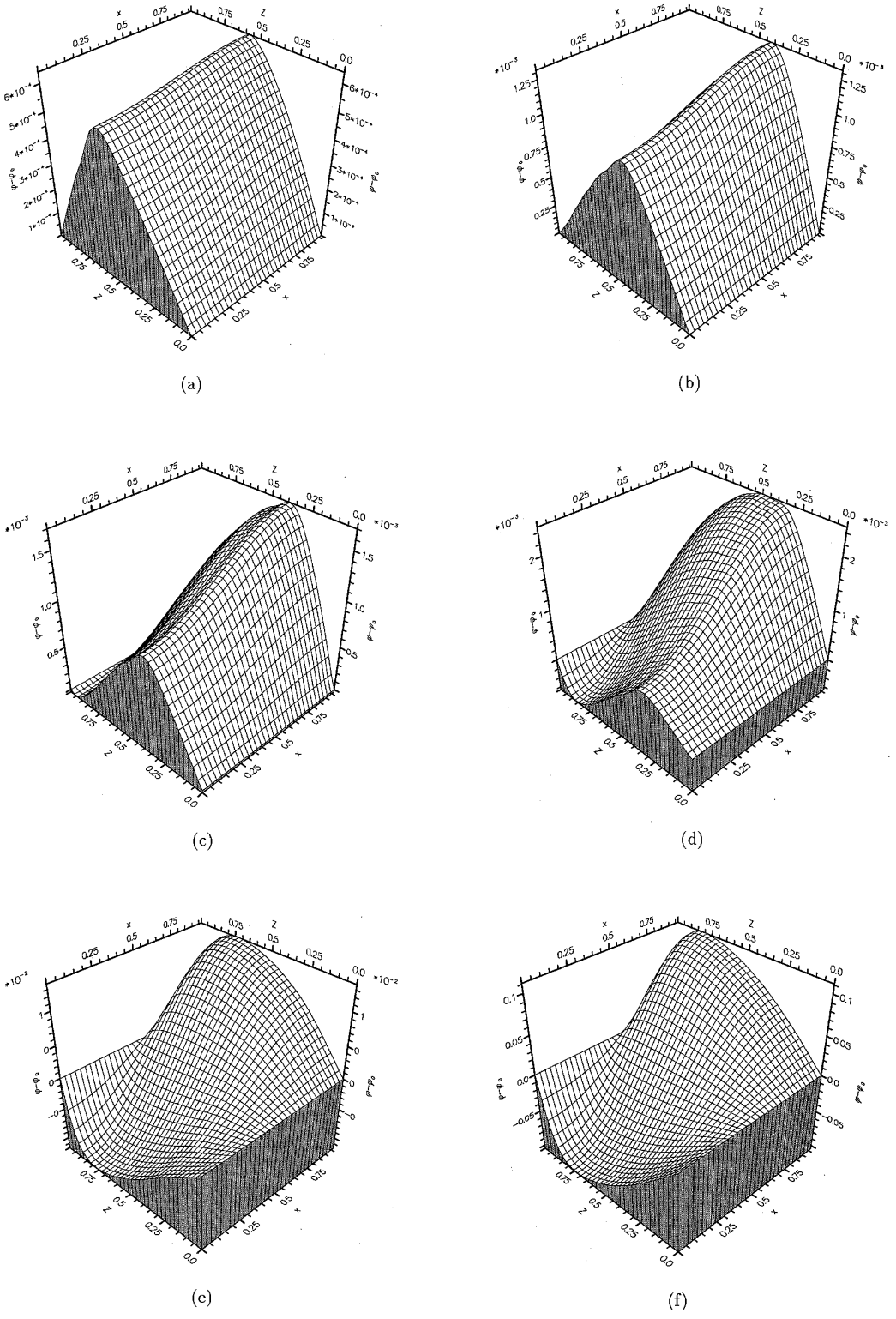

Figure 9. (a) The mass fraction difference $\phi - \phi_0$ at (a) $t = 0{\cdot}3$, (b) $t = 0{\cdot}7$, (c) $t = 0{\cdot}9$, (d) $t = 1{\cdot}1$, (e) $t = 1{\cdot}5$, (f) $t = 1{\cdot}9$. The initial data was the same as in Figure 8.

In Figure 9 the evolution of the mass fraction is depicted. Little deviation is expected initially from the non-convective solution, so the results are presented as the difference from the similarity solution ϕ_0. Initially at $t = 0{\cdot}3$ (Figure 9(a)) the solution is dominated by the local discretisation error for the diffusive terms, even though linear stability predicts convection to have been initiated. In Figure 9(c) there is some x-variation which suggests that convection has started. Solute-rich fluid rising on the left side of the cell decreases the mass fraction of solid, while falling solute-depleted fluid on the right increases the solid mass fraction. Gradually the effects of convection become more pronounced (Figures 9(d–f)) until eventually at $t \sim 2 \cdot 0$ the simulation fails to find a solution to the difference equations. In the steady case it is known that, once ϕ becomes negative, the solution fails to exist by a maximum principle [16]. Thus, in the current simulation we suspect that, once $\phi < 0$ at some time $t = t_f^N$, the solution no longer exists, and therefore the numerical scheme will 'blow-up'. Indeed, if we plot ϕ at two times before the end of the simulation (Figures 10(a,b)), we can see that ϕ is negative at the mush/liquid interface $(Z = 1)$, and a channel appears to grow down into the mush. This is observed experimentally by Tait and Jaupart [4]. However, it should be remembered that our mathematical model is invalid as soon as $\phi < 0$. We might consider the mush interface to be now on $\phi = 0$, and specify the other appropriate interfacial boundary conditions there. Unfortunately, we have assumed a particular structure for the flow in the liquid region. When $\phi < 0$, the convection is shown experimentally to be dominated by the flow out of the chimneys, obliterating the finger-like structure in the liquid. Consequently, we must reformulate our model if we wish to follow the development of a channel within the mush.

7. Further results

From the sequence of graphs 8–10 it is difficult to ascertain exactly when convection starts. Near the beginning of the simulation the stream function is very small, its magnitude being determined by the initial perturbation. To gauge the strength of convection we introduce the 2-norm defined by

$$||\psi|| = \left(\int_0^1 \int_0^1 |\psi|^2 \, \mathrm{d}x \, \mathrm{d}Z \right)^{1/2}. \tag{7.1}$$

Thus for $t \sim t_s$, $||\psi|| \sim \epsilon$, where ϵ is the initial perturbation. If we suppose that growth (or decay) is locally exponential (in time) of the form $\mathrm{e}^{\sigma t}$, then the local growth rate is

$$\sigma = \frac{1}{\delta t} \log \left[\frac{||\psi(t + \delta t)||}{||\psi||} \right], \tag{7.2}$$

where δt is some small time perturbation. In particular we can use the criterion $\sigma > 0$ for the onset of convection in the mush. In terms of the finite-difference schemes, we use the trapezium rule to approximate (7.1) giving

$$||\psi|| \approx h^2 \left[\frac{1}{2} \sum_{i=1}^{N_x - 1} (\psi_{i,M}^n)^2 + \sum_{j=1}^{M-1} \sum_{i=1}^{N_x - 1} (\psi_{i,j}^n)^2 \right]. \tag{7.3}$$

The time perturbation δt was typically taken to be ten time steps in order to help smooth numerical noise.

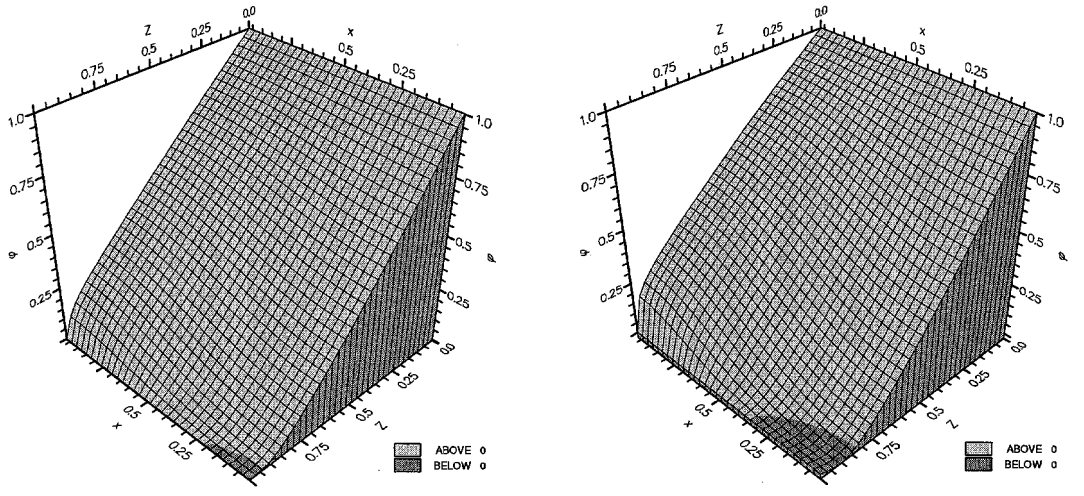

(a) (b)

Figure 10. (a) The mass fraction of solid ϕ at (a) $t = 1{\cdot}9$, (b) $t = 2{\cdot}0$. The initial data was the same as in Figure 8.

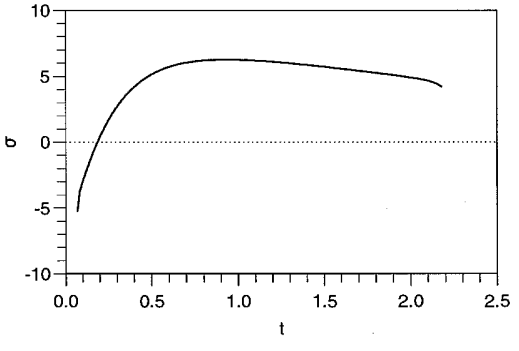

Figure 11. The growth rate σ as a function of t for $d_w = 2{\cdot}0$, $\Delta_\infty = 1{\cdot}6$, $\Delta t = 10^{-2}$, $h = \frac{1}{16}$, $\epsilon = 10^{-5}$, $t_s = 0{\cdot}05$.

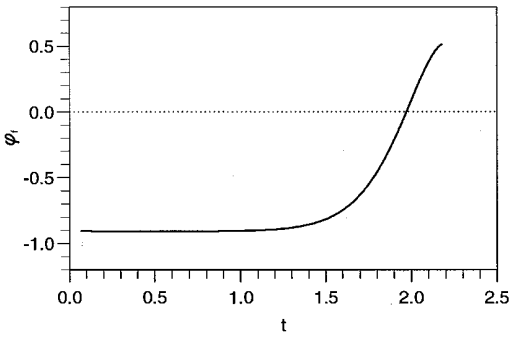

Figure 12. The evolution of ϕ_f. Initial data was the same as in Figure 11.

The onset of freckling has been defined to occur when $\phi < 0$. However, this is not the most convenient form for a finite-difference scheme. If we define

$$\phi_f = \max_{0<x<1} \left(-\frac{\phi(x, 1-h, t)}{h} \right), \tag{7.4}$$

then to leading order ϕ_f is independent of the grid spacing h. The condition for the onset of freckling is now $\phi_f > 0$. In Figures 11 and 12 we plot σ and ϕ_f for the same initial data as the time series in the Section 6. As is evident from Figure 11, the initial perturbation $\epsilon = 10^{-5}$ decays until at $t \sim 0{\cdot}18$, $\sigma > 0$ and convection begins. Growth is then approximately exponential with $\sigma \sim 5$, until at $t \sim 2{\cdot}2$ the simulation terminates. From Figure 12 we see that convection has little effect on the mass fraction right up to $t \sim 1{\cdot}5$. At $t \sim 1{\cdot}9$, $\phi_f > 0$, and hence we predict channel formation. In one further plot (Figure 13) we show the variation of ϕ_f with $||\psi||$. Notice how $||\psi||$ remains small throughout the simulation, and barely reaches

0·02 before the program terminates. This tends to support the supposition that the solution to the problem does not exist for $\phi_f > 0$, and we are not witnessing numerical instability.

A fundamental requirement of any finite-difference scheme is that the solution produced should be independent of the grid spacing. We can use the growth rate σ, and the freckling parameter ϕ_f to assess the dependence for the fully implicit scheme. In Figure 14(a,b) we plot σ and ϕ_f against time for $h = \frac{1}{16}, \frac{1}{32}, \frac{1}{48}$. There is very good agreement for the growth rate over the entire simulation. Indeed all three runs gave the onset of convection as $t_c^N \sim 0{\cdot}18$. We use a superscript N to denote values obtained from the numerical simulation. The agreement is not so good for ϕ_f, especially near the end of the simulation.

We can make another check on the schemes by fixing the interface and only consider the temperature and stream function in the mush. The equations are then effectively those for convection in a porous medium for which it is known that the critical Rayleigh number is $R_c \sim 27{\cdot}1$ [28]. Here the equivalent Rayleigh number is sR. The onset of convection was determined numerically in this case to occur when $sR \sim 27$, further validating the schemes.

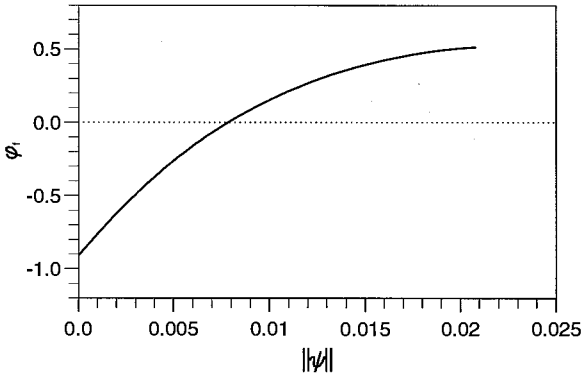

Figure 13. The variation of ϕ_f with $||\psi||$. Initial data was the same as in Figure 11.

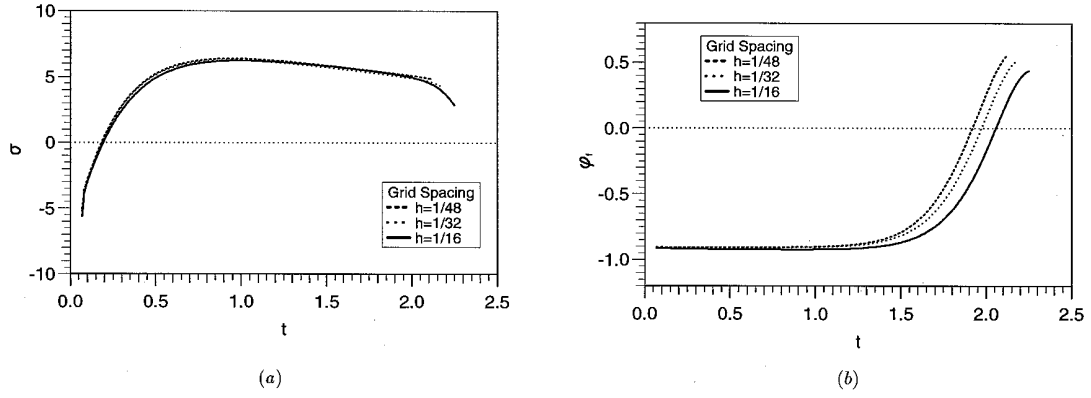

Figure 14. (a) The effect of mesh refinement on (a) the growth rate σ, and (b) on ϕ_f for $d_w = 2{\cdot}0$, $\Delta_\infty = 1{\cdot}6$, $\Delta t = 10^{-3}$, $t_s = 0{\cdot}05$, $\epsilon = 10^{-5}$.

Table 2. The effect of varying the width of the horizontal domain d_w with initial data $\Delta_\infty = 1{\cdot}6$, $h = \frac{1}{32}$, $\epsilon = 10^{-5}$, $d_w^2 t_s = 0{\cdot}4$, $d_w^2 \Delta t = 4 \times 10^{-3}$.

Domain width d_w	Onset of convection $d_w^2 t_c^N$	Onset of freckling $d_w^2 t_f^N$
1·0	—	—
2·0	0·69	7·46
3·0	0·62	8·10
4·0	0·62	9·38

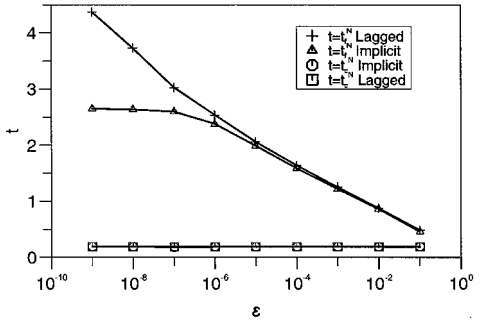

Figure 15. A comparison of the lagged and fully implicit schemes. Initial data for the lagged scheme was $d_w = 2{\cdot}0$, $\Delta_\infty = 1{\cdot}6$, $\Delta t = 2 \times 10^{-4}$, $h = \frac{1}{16}$, $t_s = 0{\cdot}5$. For the implicit scheme the time step was increased to $\Delta t = 10^{-3}$.

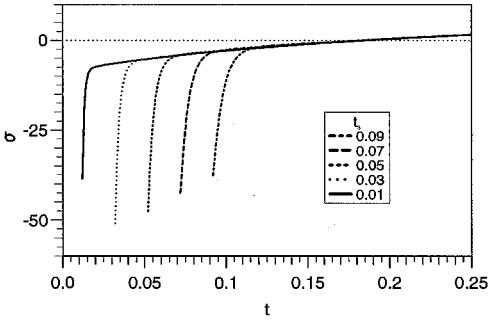

Figure 16. The growth rate σ for different start times t_s. Initial data was $d_w = 2{\cdot}0$, $\Delta_\infty = 1{\cdot}6$, $h = \frac{1}{16}$, $\epsilon = 10^{-5}$, $\Delta t = 10^{-3}$.

7.1. INITIAL CONDITIONS

In this section we determine the dependence of the convection time t_c^N and the freckling time t_f^N on the initial conditions. Clearly, there will be some effect on the subsequent solidification if the initial perturbation is sufficiently large. We plot t_c^N and t_f^N against ϵ using each scheme for $h = \frac{1}{16}$ in Figure 15. A coarser mesh was used because each point represents a separate simulation, which means that the computational cost rises. For $\epsilon = 10^{-9}, 10^{-8}, 10^{-7}$ the onset of convection could only be estimated from the curve $\sigma = \sigma(t)$. A large amount of numerical noise made this difficult, so these points are speculative. The two schemes gave approximately the same value of t_c^N, irrespective of the initial perturbation (with the above proviso). This suggests that the bifurcation to the convective state is supercritical in line with the results of the nonlinear stability analysis. However, the onset of channels clearly depends strongly on the initial perturbation. For small ϵ there is considerable disagreement between the schemes. The fully implicit scheme shows the expected tendency of $t_f^N \to$ const. as ϵ becomes small, since then the truncation error is bigger than ϵ. The lagged scheme does not appear to model the coupling between ϕ, T, and p as well, so in future we restrict attention to the fully implicit scheme. We obtain similar results by varying the start time t_s (Figure 16). Changing the t_s is tantamount to changing the initial perturbation. A larger value of T_s means $||\psi||$ will be larger at the onset of convection, hence significantly diminishing the time for freckles to form.

Table 3. The onset of convection in the mush with $d_w = 2{\cdot}0$, $\Delta t = 10^{-3}$, $h = \frac{1}{16}$, $\epsilon = 10^{-5}$, $t_s = 0{\cdot}05$.

Δ_∞	α	$d_w^2 t_c$ (linear stability)	$d_w^2 t_c^N$ (simulation)	R_c^N	R_c	k_c
0·1	1·1205	0·448	0·333	12·93	15·00	1·74
0·3	0·8090	0·510	0·332	9·32	11·56	1·59
0·6	0·6075	0·623	0·336	7·04	9·59	1·48
1·0	0·4666	0·806	0·452	6·27	8·38	1·39
1·6	0·3503	1·146	0·748	6·06	7·50	1·31
3·0	0·2238	2·253	1·932	6·22	6·72	1·21
6·0	0·1270	6·094	6·660	6·55	6·27	1·14
10·0	0·0807	14·439	—	—	6·13	1·11
∞	0	∞	—	—	6·03	1·09

For domains of greater width we resort to a finer mesh $h = \frac{1}{32}$ in an attempt to preserve accuracy. A number of results for differing cell widths are shown in Table 2. A square domain $(d_w = 1)$ did not give rise to convection, and hence there was no freckling. Note that the times are multiplied by d_w^2 to reflect the initial scaling made in Equation (5.2). The onset of convection was not greatly affected by the width of the horizontal domain, but the onset of freckling was more strongly influenced. The results show that a wider mold will significantly inhibit freckling, which is somewhat contrary to experimental evidence. It should be remembered, however, that the initial perturbation (5.4) assumed a single convection cell. For larger values of d_w a number of convection cells form. This means that an additional time is needed to adjust to the correct form of solution, which delays the initiation of channelling.

7.2. A COMPARISON WITH LINEAR STABILITY THEORY

Linear stability calculations for the initiation of convection were presented in EF as a function of the superheat Δ_∞. In this section we compare those results with the present numerical calculations. In Table 3 we have tabulated a number of results for differing superheats. From the linear stability analysis the critical Rayleigh number R_c, and the critical wave number k_c were calculated. The critical wavelength is given by

$$\lambda_c = \frac{2\pi R_c}{k_c R}, \tag{7.5}$$

and the time for the onset of convection is

$$d_w^2 t_c^N = \frac{R_c^2}{4\alpha^2 R^2}. \tag{7.6}$$

The initial data for each run is given in the caption to the figure. A plot of the numerical results for the critical Rayleigh number R_c is shown in Figure 17. Increasing superheat appears to delay the onset of convection as has been noted by Worster [29]. Also shown on Figure 17 are the linear stability results from EF. For large values of Δ_∞ a numerical solution is not feasible with the present scheme. Indeed, to compute the results for $\Delta_\infty = 6{\cdot}0$ we require $F = 20$,

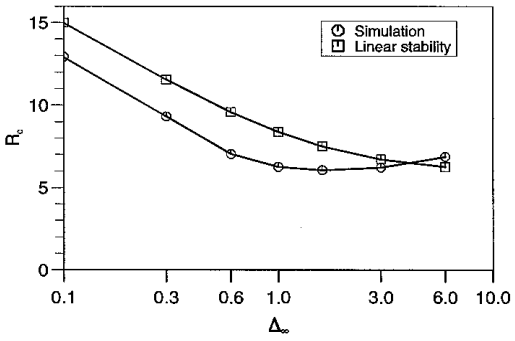

Figure 17. A comparison of the critical Rayleigh number for convection in the mush as predicted by the linear stability analysis, and the numerical simulation. For each point $d_w = 2{\cdot}0$, $\Delta t = 10^{-2}$, $h = \frac{1}{16}$, $\epsilon = 10^{-5}$, $t_s = 0{\cdot}05$.

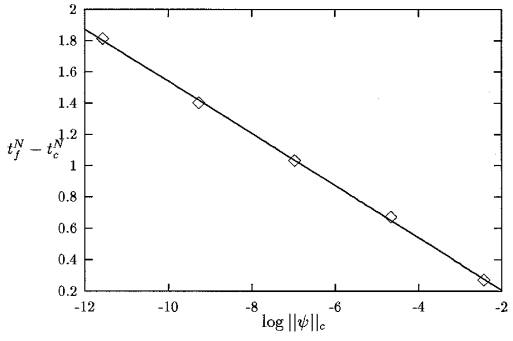

Figure 18. The effect of varying the initial perturbation to the similarity solution on the onset of freckles. Initial data was the same as in Figure 15.

with a correspondingly large increase in computational time. In the stability analysis of EF it was found that $R_c \to$ const. as $\Delta_\infty \to \infty$. Here, R_c^N increases at large superheat, even though t_c^N is still increasing. Generally, the numerical results predict the onset of convection earlier (initial conditions have little effect). We can take this as a consequence of the quasi-steady approximation. However, it is reassuring to note that the results are qualitatively similar.

7.3. THE ONSET OF CHANNELLING

It was established in Section 7.1 that the freckling time depended strongly on the initial perturbation. We will now establish the form of the dependence. More generally (not just for exponential growth), we define the local growth (or decay) rate to be

$$\sigma = \frac{1}{||\psi||}\frac{\mathrm{d}||\psi||}{\mathrm{d}t}. \tag{7.7}$$

On integration we obtain

$$||\psi|| = ||\psi||_c \exp\left[\int_{t_c^N}^{t} \sigma(t)\,\mathrm{d}t\right], \tag{7.8}$$

where $||\psi||_c = ||\psi||$ at $t = t_c^N$. If we define $T = \log||\psi||$ at $t = t_f^N$, then

$$T = \int_{t_c^N}^{t_f^N} \sigma(t)\,\mathrm{d}t + \log||\psi||_c\,. \tag{7.9}$$

From Figure 11 it can be seen that σ quickly attains a fairly constant value after the onset of convection. On assuming that $\sigma = \sigma^*$ is constant, we find that (7.9) becomes

$$t_f^N - t_c^N = \frac{T - \log||\psi||_c}{\sigma^*}. \tag{7.10}$$

We plot $t_f^N - t_c^N$ against $\log ||\psi||_c$ for $\Delta_\infty = 1{\cdot}6$ in Figure 18. The assumption of constant growth rate appears to be a very good approximation. A best fit straight line was calculated to be

$$t_f^N - t_c^N = -0{\cdot}13 - 0{\cdot}17 \log ||\psi||_c \,, \tag{7.11}$$

which gives $\sigma^* \sim 6$ (*cf.* Figure 11). Thus, (7.11) gives the freckling time as a function of the initial perturbation; the onset of convection remains constant at $t_c^N \sim 0{\cdot}18$ for $\Delta_\infty = 1{\cdot}6$.

Careful experimentation should lead to very small initial perturbations. Therefore, a value for the freckling time might reasonably be taken as the maximum time predicted by the implicit scheme, that is $d_w^2 t_f^N \sim 10{\cdot}4$ (Figure 15). If we use the similarity solution to define a Rayleigh number for the onset of freckles, then

$$R_f^N = 2\alpha d_w \sqrt{t_f^N}\, R. \tag{7.12}$$

For $R = 10$, we find $R_f \sim 22{\cdot}6$. Such a value can only be a crude estimate for the time at which channels might be visible in experiments, since R is usually an order of magnitude larger. However, the figure does not seem unreasonable given that the critical Rayleigh number for freckling recorded experimentally ranges from 20 to 250 [4, 30]. Indeed, experiments have yet to distinguish the convective instability from the onset of channelling, primarily due to difficulty of making observations in the mush.

8. Conclusions

Stable weakly nonlinear solutions appropriate to convection in a solidifying mushy layer have been derived. These are able to predict the onset of freckling, but only outside the range of the validity of the asymptotic expansions. Thus we solved the alloy model numerically, using a front-fixing transformation. We aimed to complement the Rayleigh-number criterion for convective instability in the mush, with a Rayleigh-number criterion for freckle formation (as suggested by Fowler [16]). From the numerical simulation we found that this is not possible, because freckle formation is strongly influenced by the initial conditions. Thus, we can only stipulate a critical Rayleigh number for freckling at which very small initial perturbations to the convective state lead to channelling. It appears that the best way to prevent freckles from forming is to prevent the onset of convection in the mush (*e.g.* by some stirring mechanism).

The two numerical schemes describe one way of solving the moving-boundary problem that arises out of alloy solidification. They are not necessarily the best way, but they do enable the first theoretical computations to be made for freckle formation. Of course, we could improve the efficiency of the schemes by introducing a variable time step or mesh size. The time step must be sufficiently small near $t = t_s$ to model accurately the large change in the interface position. However, later on in the simulation there is no reason why the time step could not be increased. A variable grid spacing would allow more nodes to be placed near the interface, and fewer near $Z = F$. This would decrease computation time considerably, since at present the routine spends most of its time finding the temperature in the liquid region. These measures would, however, complicate an already laborious solution procedure.

The independence of the onset of convection with the magnitude of the initial perturbation would seem to be at odds with the hypotheses of Amberg and Homsy [9]. They predicted a subcritical bifurcation from the convection-less state with the chimney flow régime as the

appropriate solution, once the flow was sufficiently rapid. Here, the numerical simulation predicts a supercritical bifurcation in agreement with the nonlinear stability analysis in Sections 3 and 4. However, it should be remembered that Amberg and Homsy allowed the permeability to be a function of porosity, whereas in the reduced model (2.3)–(2.7) permeability is assumed constant.

The analysis presented herein was guided by the solidification of ammonium-chloride solution. Recently, Huppert [31] has case some doubt as to whether results obtained from the study of this solution can be extrapolated to metal binary alloys. Many other aqueous salt solutions exhibit the same convective flow patterns as are found in the solidification of ammonium chloride. Yet, rarely do other aqueous solutions form the distinctive chimneys structures visible in the mush. This may be due to the low entropy of fusion of ammonium-chloride solution in common with metal alloys, or the fact that it forms non-faceted (and thus truly dendritic) unhydrated crystals. Huppert and Hallworth [32] have noticed that the tendency to form freckles is reduced if copper sulphate is added to the solution. This makes the crystals more faceted and so might explain the special properties of ammonium chloride. However, Worster and Kerr [33] have recently suggested that the addition of copper sulphate increases the undercooling at the mush/liquid interface, which in turn lowers the Rayleigh number for the mush. Clearly this problem has not yet been fully resolved.

Acknowledgements

I would like to thank Andrew Fowler for his help during the course of this work. This research was supported by the award of an SERC research studentship.

References

1. M. C. Flemings, *Solidification Processing*. New York: McGraw-Hill (1974) 364pp.
2. S. M. Copley, A. F. Giamei, S. M. Johnson and M. F. Hornbecker, The origin of freckles in unidirectionally solidified castings. *Metall. Trans.* 1 (1970) 2193–2204.
3. W. W. Mullins and R. F. Sekerka, Stability of a planar interface during solidification of a dilute binary alloy. *J. Appl. Phys.* 35 (1964) 444–451.
4. S. Tait and C. Jaupart, Compositional convection in a reactive crystalline mush and melt differentiation. *J. Geophys. Res.* 97(B5) (1992) 6735–6756.
5. M. G. Worster, Convection in mushy layers. *Ann. Rev. Fluid Mech.* 29 (1997) 91–122.
6. J. S. Turner, *Buoyancy Effects in Fluids*. Cambridge: Cambridge University Press (1973) 367pp.
7. P. W. Emms and A. C. Fowler, Compositional convection in the solidification of binary alloys. *J. Fluid Mech.* 262 (1994) 111–139.
8. M. G. Worster, Solidification of an alloy from a cooled boundary. *J. Fluid Mech.* 167 (1986) 481–501.
9. G. Amberg and G. M. Homsy, Nonlinear analysis of buoyant convection in binary solidification with application to channel formation. *J. Fluid Mech.* 252 (1993) 79–98.
10. M. G. Worster, Instabilities of the liquid and mushy regions during solidification of alloys. *J. Fluid Mech.* 237 (1992) 649–669.
11. S. Tait, K. Jahrling and C. Jaupart, The planform of compositional convection and chimney formation in a mushy layer. *Nature* 359(6394) (1992) 406–408.
12. D. M. Anderson and M. G. Worster, Weakly nonlinear analysis of convection in mushy layers during the solidification of binary alloys. *J. Fluid Mech.* (1995) 307–331.
13. D. G. Neilson and F. P. Incropera, Unidirectional solidification of a binary alloy and the effects of induced fluid motion. *Int. J. Heat Mass Transf.* 34 (1991) 1717–1732.
14. D. G. Neilson and F. P. Incropera, Effect of rotation on fluid motion and channel formation during unidirectional solidification of a binary alloy. *Int. J. Heat Mass Transf.* 36 (1993) 485–505.
15. S. D. Felicelli, J. C. Heinrich and D. R. Poirier, Simulation of freckles during vertical solidification of binary alloys. *Metall. Trans.* 22B (1991) 847–859.
16. A. C. Fowler, The formation of freckles in binary alloys. *IMA J. Appl. Math.* 35 (1985) 159–174.

17. R. N. Hills, D. E. Loper and P. H. Roberts, A thermodynamically consistent model of a mushy zone. *Q. J. Mech. Appl. Math.* 36 (1983) 505–539.
18. P. W. Emms, *Compositional Convection and Freckle Formation in the Solidification of Binary Alloys*. D. Phil. Thesis, Oxford University (1993).
19. J. L. Robinson, A note on the stability of an infinite fluid heated from below. *J. Fluid Mech.* 20 (1967) 461–464.
20. T. D. Foster, Stability of a homogeneous fluid cooled uniformly from above. *Phys. Fluids* 8 (1965) 1249–1257.
21. G. M. Homsy, Global stability of time-dependent flows: impulsively heated or cooled fluid layers. *J. Fluid Mech.* 60 (1973) 129–139.
22. J. Crank, *Free and Moving Boundary Problems*. Oxford: Clarendon Press (1984) 425pp.
23. N. B. Esikova, O. P. Iliev and P. N. Vabishchevich, Numerical investigation of convection/diffusion phase change of a metal with temperature-dependent viscosity. *Comm. Appl. Num. Meth.* 8 (1992) 857–868.
24. J. L. Robinson, Theoretical analysis of convective instability of a growing horizontal thermal boundary layer. *Phys. Fluids* 19 (1976) 778–791.
25. A. C. Newell and J. A. Whitehead, Finite bandwidth, finite amplitude convection. *J. Fluid Mech.* 38 (1969) 279–303.
26. A. A. Wheeler, Some aspects of the weakly non-linear theory of the morphological instability. *IMA J. Appl. Math.* 35 (1985) 131–144.
27. P. G. Drazin and W. H. Reid, *Hydrodynamic Stability*. Cambridge: Cambridge University Press (1981) 525pp.
28. D. A. Nield, Onset of thermohaline convection in a porous medium. In: S. Kabac *et al.* (eds), *Convective Heat and Mass Transfer in Porous Media*. Dordrecht: Kluwer Academic Publishers (1991) pp. 79–122.
29. M. G. Worster, The dynamics of mushy layers. In: S. H. Davis, H. E. Huppert, U. Müller and M. G. Worster (eds), *Interactive Dynamics of Convection and Solidification*. Dordrecht: Kluwer Academic Publishers (1992) pp. 113–138.
30. C. F. Chen and F. Chen, Experimental study of directional solidification of aqueous ammonium chloride solution. *J. Fluid Mech.* 227 (1991) 567–586.
31. H. E. Huppert, The fluid mechanics of solidification. *J. Fluid Mech.* 212 (1990) 209–240.
32. H. E. Huppert and M. A. Hallworth, Solidification of NH_4Cl and NH_4Br from aqueous solutions contaminated by $CuSO_4$: the extinction of chimneys. *J. Crystal Growth* 130 (1993) 495–506.
33. M. G. Worster and R. C. Kerr, The transient behaviour of alloys solidified from below prior to the formation of chimneys. *J. Fluid Mech.* 269 (1994) 23–44.